Journal of Applied Fluid Mechanics, Vol. 16, No. 4, pp. 671-684, 2023.
Available online at www.jafmonline.net, ISSN 1735-3572, EISSN 1735-3645.
https://doi.org/10.47176/jafm.16.04.1532

Drag Reduction Performance of Triangular (V-groove) Riblets with Different Adjacent Height Ratios

Z. M. Liu[1,2], R. Chen[1], Z. Q. Tang[3], Q. Tian[1], Y. C. Fang[1], P. J. Li[1], L. Li[1]and Y. Pang[1,2†]

[1] *Faculty of Materials and Manufacturing, Beijing University of Technology, Beijing 100124, China*
[2] *Beijing Key Laboratory of Advanced Manufacturing Technology, Beijing University of Technology, Beijing 100124, China*
[3] *School of Mechanical Engineering, Tianjin University, Tianjin 300072, China*

†*Corresponding Author Email: pangyan@bjut.edu.cn*

(Received September 20, 2022; accepted December 13, 2022)

ABSTRACT

Surface structure is used to interfere with the turbulent boundary layer in the groove drag reduction, which is important to the endurance and stability of high-speed and ultrahigh-speed aircraft. The size of the groove structure directly affects the flow in the turbulent boundary layer and changes the drag reduction effect. The drag reduction characteristics of bionic triangular (V-groove) riblets were studied through Particle Image Velocimetry (PIV) experiment and Finite Volume Method (FVM) simulation. Triangular riblets with adjacent height ratios (AHR) of 1.00, 1.74, and 3.02 were considered in this research, and the influence of these groove structures on the flow characteristics of turbulence near the wall is compared with those of the smooth plates. The distribution of time-averaged velocity, turbulence intensity, and coherent structures of turbulent boundary layer on the riblet surface is analyzed to document the effects of the geometric parameters of various groove structures on drag reduction rates. Results showed that the best drag reduction is obtained using the V-groove riblets with adjacent height ratio of 1:1 under the low free-stream velocity. The results can be used as a reference for further optimization of drag reduction structures with surface grooves.

Keywords: Turbulent channel flow; Riblet surface; Adjacent height ratio; PIV.

NOMENCLATURE

AHR	Adjacent Height Ratio	u_∞, U_e	free-stream velocity
RSS	Reynolds Shear Stress	τ_w	magnitude of wall shear stress
TKE	Turbulent Kinetic Energy	Re_L	Reynolds number
TBL	Turbulent Boundary Layer	u_x, u_y, u_z	velocity values in three directions
WSS	Wall Shear Stress	w_x, w_y, w_z	vorticity values in three directions
ISQM	Improved Quadrant Splitting Method	$\|w\|$	magnitude of vorticity
JPDF	Joint Probability Density Function	α	opening angle of h_1
L, W, H	test section: length, width, height	β	opening angle of h_2
H_0	threshold of $u'v'$	ν	kinematic viscosity
B	constant based on exp-results	μ	molecular (dynamic) viscosity
ΔB	upward shift of log velocity profile	ρ	air density
C_D	drag coefficient of the TBL	η	drag reduction rate
C_f	mean skin friction coefficients	κ	von Kármán constant
X^+, Y^+	dimensionless displacement	γ	Euler constant
x, y, z	three components of displacement	ψ	digamma function
h, s	height and width of riblets	δ	channel half-height
h^+, s^+	dimensionless shape of riblets	$-R<u',v'>$	magnitude of the RSS
u', v'	fluctuating velocity	$u'v'P(u', v')$	integral of covariance integrand
h_1, h_2	height of riblets	$\sqrt{\overline{u'^2}}/U_e$	streamwise turbulent intensity
$h_p=y_0$	protrusion height	$\sqrt{\overline{v'^2}}/U_e$	wall-normal turbulent intensity
u_τ	friction velocity		

1. INTRODUCTION

In bionic groove drag reduction technology, a regular microstructure according to the biological surface is designed to reduce flow resistance by controlling the turbulent structure of the boundary layer (Yu *et al.* 2020) and decreasing the turbulent kinetic energy (TKE). This method has the advantages of simplicity, low energy consumption, and low cost; thus, it is widely used in aerospace, transportation, industrial manufacturing, and other fields (Nili-Ahmadabadi *et al.* 2019). Passive drag reduction methods using streamwise riblet surfaces are partly inspired by the natural ribbed surfaces observed in sharks (Kumar *et al.* 2021), whose riblet-textured surfaces achieve drag reduction by affecting the flow field patterns and loss of the turbulent kinetic energy in the turbulent boundary layers (TBLs). The analysis of the mechanism of near-wall turbulence structures for drag reduction on the riblet surfaces has theoretical guidance for improving energy efficiency.

Since NASA Langley Research Center first confirmed that streamwise riblet surfaces can effectively reduce surface friction resistance, riblet drag reduction has always been a research hotspot in the field of drag reduction. To understand the dynamical effects of the riblet wall geometry on the flow field, riblets with different height-to-spacing ratios have been studied by Walsh (1980) and Xu *et al.* (2018), showing that the groove surface has the effect of drag reduction. In addition, the optimal drag reduction rate is 8% when the dimensionless height is $h^+ \leq 25$ ($h^+ = hu_\tau/\nu$) and the dimensionless spacing is $s^+ \leq 30$ ($s^+ = su_\tau/\nu$), where ν indicates the kinematic viscosity. Subsequently, Bai *et al.* (2016a), Bechert and Bartenwerfer (1989), and Qiu *et al.* (2020) further studied the flow resistance of walls with the blade, sawtooth, and scalloped riblet surfaces by numerical simulations. They found that the optimal geometry includes typical blade-type structures but less mechanically robust than V- or U-type cross sections. Nowadays, a recurrent theme of passive drag reduction has turn into the bionics field. Inspired by shark skin replica, Jung and Bhushan (2010) carried out particle image velocimetry (PIV) experiments on a rib-patterned surface to simulate shark skin structure, and they found that it had evident drag-reducing ability. Furthermore, Feng *et al.* (2015) conducted a comparative study on the herringbone riblets of feather using wind tunnel and numerical simulation methods. They revealed that the shape of the riblets reduces the Reynolds stress on the patterned rib surface and achieves drag reduction. El-Samni *et al.* (2007) studied the turbulence for a uniformly distributed thin rectangular riblet surface at low Reynolds number by direct numerical simulation (DNS). They showed that the maximum drag reduction obtained is approximately 11%, which occurs at a spacing of 18 s^+, whereas the drag increased when the spacing is larger than 30 s^+. Most previous studies have used the triangular riblets by developing artificial 2D geometries constructed based on a 2D shark skin image. However, studies on the influence of non-equal height microstructure of actual sharkskin denticles and staggered layout on local turbulent flow properties in terms of vortices and shear stresses are still very few.

The research on the drag reduction mechanism of turbulence along the riblet plates should rely on the analysis of the flow field structure near the wall. Samik Bhattacharya and Ahmed (2020), through surface flow visualization study of the wind tunnel, showed the strong influence of aspect ratio on the near wall flow upstream and in the wake of the models vividly observed from the trajectories of the limiting streamlines. Modesti *et al.* (2021) studied the near-wall streamwise vortical structures and the spanwise flow of the low-velocity strip and argued that the secondary vortices with opposite direction for the streamwise vortices are the main factors for drag reduction. This condition limits the spanwise translation of the flow vortex and weakens the frequency and intensity of the bursting events, thereby decreasing the skin-friction drag. Wu *et al.* (2019) proposed *the Air Rolling Bearing Theory* by studying the flow patterns on the near-wall of various riblet surfaces and analyzing the drag reduction feature of microgroove surface, indicating a stable formation of the low-velocity vortex at the valley of riblets when the fluid flows along the spanwise direction. The low-velocity vortex has a similar principle to *the Secondary Vortex Group Theory*, enabling the fluid to contact the low-velocity vortex merely. As a result, the magnitude of the shear stress at the wall is reduced, the energy transfer process is hindered, and drag reduction is achieved. However, Boomsma and Sotiropoulos (2016) found through DNS simulation that secondary vortices also appear on the surface with the microstructure under the drag-increasing condition, thereby confirming that secondary vortices might not be the main reason for drag reduction. Joshi and Bhattacharya (2019) conducted large eddy simulation (LES) to show that geometry variation created spatially locked streamwise vortices, which disrupted regular vortex shedding to the form drag. Based on the *Highlighting Theories* proposed by Bechert and Bartenwerfer (1989), the velocity distribution of riblets for the near-wall region was analyzed by Zhang *et al.* (2020a) and showed that riblet troughs generally caused less velocity gradient owing to the interaction of vortices with the ridge plane under the virtual origin. The low-velocity fluid, which restrains the translation of the transverse flow and fluctuating velocity, is concentrated within the riblets. Therefore, the riblet tips above the virtual origin bear higher magnitude of the wall shear stress, whereas the riblet valleys have minimum shear stress. Chen *et al.* (2013) found that the thickening of the viscous sublayer, which arises from low-velocity area near the wall, pushes the transition buffer layer and log-law layer outward and causes drag reduction on the riblet plates. Rastegari and Akhavan (2018) and Mele and Tognaccini (2018) modeled the groove structure and found that the flow field and the drag-reducing ability of V-grooves can be effectively matched by those of the smooth plates with the slip-boundary condition. However, finding an acceptable relationship of slip velocity with other drag reduction theories is difficult. Although the drag reduction of

the turbulence can be explained through the existing theories from different point of views, unified theories to interpret the cause of drag-reducing shark skin and its turbulent structure are unavailable, and further research is required.

Although the drag reduction of different shapes and arrangements of riblets is performed through various previous experiments and numerical studies on turbulent flows (Li 2020; Zhang *et al.* 2020a), some studies only focused on the thickening of the viscous sublayer near the riblet side, and they lacked an in-depth discussion on the relation between turbulent vortex structures and turbulence statistics on the riblet side. In addition, although riblet shapes with different heights have been proposed by Chen *et al.* (2014) and Miyazaki *et al.* (2018), they have not been systematically investigated from the perspective of experiment and simulation. Inspired by the research on Bionics of Galapagos shark skin digital model, the present work studies gas flow on a smooth surface and uses the three other riblet-surface models with adjacent height ratios of 1.00, 1.74, and 3.02 by PIV experiment and numerical simulation. The velocity vector fields of the riblet plates with different AHRs and the flat (smooth) plates are photographed by CCD to analyze the influence of the riblet on the time-averaged velocity near the wall. The verified Fluent simulation method is used to further analyze the flow characteristics, including wall shear stress and drag reduction rate under the riblet shape with different AHRs (The ratio of riblet heights adjacent to each other, h_1/h_2). The turbulent characteristics and the coherent structure of these grooves are analyzed mechanically based on the quadrant splitting method (Yang and Jiang 2012; Wallace 2016).

2. MODELS AND METHODS

2.1 Models and Setup-parameters

In this section, according to the micrograph of shark skin photographed by Jung and Bhushan (2010) (Fig. 1a), the flow characteristic of the riblet shape shown in Fig. 1(b) was investigated using Fluent (Ansys Inc. USA) software. Three types of wall microstructures were designed to explore the influence of different AHRs of trenches on the drag reduction effect, as shown in Table 1.

A typical mesh of model solution domain in the near-wall region as shown in Fig. 1(c). Since the modelling case does not need to resolve the flow within the riblets, grids are reduced primarily in the near-wall region (grid resolutions in the streamwise direction for the riblet and modelling cases are kept the same).

Table 1 Microstructure Parameters

AHR(h_1/ h_2)	h_1/mm	h_2/mm	s/mm	α/°	β/°
1.00	0.87	0.87	1.00	60	60
1.74	0.87	0.50	1.00	60	90
3.02	0.87	0.29	1.00	60	120

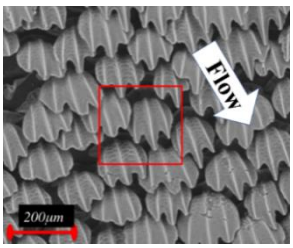

a) Micrograph of shark skin (Boomsma and Sotiropoulos 2016)

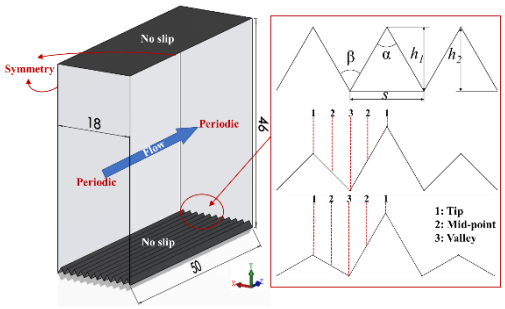

b) Computational domain and riblet shape

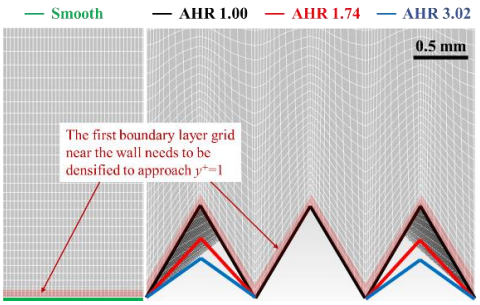

c) A typical example of the grid structure in the near-wall region

Fig. 1. Near-wall groove model structure.

The flow pattern of TBLs is essential to study the performance of turbulent drag reduction (Jung and Bhushan 2010; Feng *et al.* 2015; Bai, et al. 2016a; Heidarian *et al.* 2018,). The modeling flow field of the riblets can be used to obtain the cross-flow characteristics of the V-groove below the ridge plane, by conducting RNG k-ε computational model on the various riblet shapes at low Reynolds number. Transport Equations for the RNG k-ε Model are defined as follows:

$$\frac{\partial(\rho k)}{\partial t}+\frac{\partial(\rho k u_i)}{\partial x_i}=\frac{\partial}{\partial x_j}\left[\alpha_k \mu_{eff}\frac{\partial k}{\partial x_j}\right] +G_k+G_b-\rho\varepsilon-Y_M+S_k \tag{1}$$

$$\frac{\partial(\rho \varepsilon)}{\partial t}+\frac{\partial(\rho \varepsilon u_i)}{\partial x_i}=\frac{\partial}{\partial x_j}\left[\alpha_\varepsilon \mu_{eff}\frac{\partial \varepsilon}{\partial x_j}\right] +C_{\varepsilon 1}\frac{\varepsilon}{k}\left(G_k+C_{\varepsilon 3}G_b\right)-C_{\varepsilon 2}^{*}\rho\frac{\varepsilon^2}{k} \tag{2}$$

$$C_{\varepsilon 2}^{*}=C_{\varepsilon 2}+\frac{C_\mu \rho \eta^3(1-\eta/\eta_0)}{1+\beta\eta^3} \tag{3}$$

where G_k represents the generation of turbulence kinetic energy due to the mean velocity gradients. G_b is the generation of turbulence kinetic energy due to buoyancy. Y_M represents the contribution of the fluctuating dilatation in compressible turbulence to the overall dissipation rate. The quantities α_k and α_ε are the inverse effective Prandtl numbers for k and ε, respectively. S_k and S_ε are source terms. Other model constants are set to default parameters (Launder and Spalding 1972) in Fluent (Ansys Inc. USA) software. Besides, the boundary conditions are as follows:

1. Inlet and Outlet Boundary Conditions: Periodic boundary conditions are used for the flow direction to ensure the full development of turbulence;

2. Wall Boundary Conditions: Symmetrical boundary is adopted for both sides of the wall, and no slip is used for the top and bottom walls;

3. Solver: Pressure-based solver is used;

4. Pressure–Velocity Coupling: SIMPLEC scheme. Spatial discretization is the second-order upwind scheme, and the convergence standard is 1e-6.

5. Fluid medium: air (ρ = 1.225 kg / m^3, μ = 1.7894 $\times 10^{-5}$ kg / (m ·s)).

2.2 Experimental Platform

The experimental platform consists of a particle generator (Flow Tracker 700CE, maximum pressure 4 bar) driven by an air compressor, a wind tunnel, and a PIV system, as shown in Fig. 2(a). The experimental model is made of matt black acrylic plates with an opaque property, whose weak reflection can avoid unclear flow field image and the burnt-out CCD camera caused by laser (Fig. 2b). Olive oil is used as the fluid medium in the particle generator because it satisfies the general requirements of the PIV system, including non-corrosive, non-toxic, chemically non-volatile, and non-abrasive properties. The air flow in the wind tunnel consists of the chamber, contraction section, test section, diffuser, and fan successively, with specific sizes, as shown in Table 2. Wire mesh honeycomb is set in the chamber to filter the large-scale eddy structures (Yang *et al.* 2021), attain the steady fluid, and reduce the turbulence intensity. The contraction section satisfies the bicubic curve distribution with 6.8 ratios (Fang *et al.* 2001) to control the free-stream velocity required by the experiment. The test section is made of transparent acrylic sheet to observe air flow with tracer particles. The diffusion angle of the upper and lower walls of the diffuser section is 6°, which converts the kinetic energy of the air flow into pressure energy to reduce the power loss of the wind tunnel. The diffuser and fan are combined by a soft connection with a layer of filter screen to reduce the interference of fan's vibration to the flow field in the test section. The air flow is driven by the fan with an alternating current (AC) fan governor during the experiment.

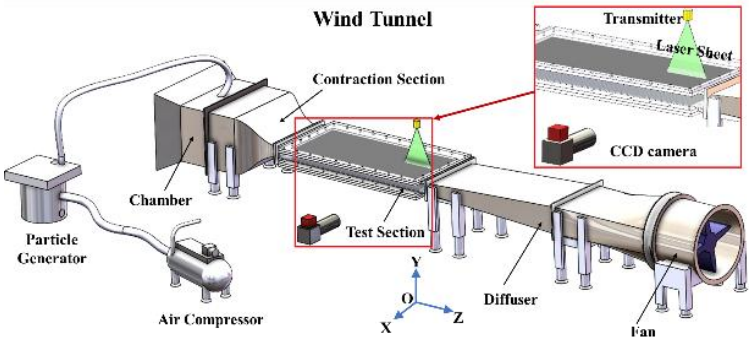

a) Wind tunnel experimental system

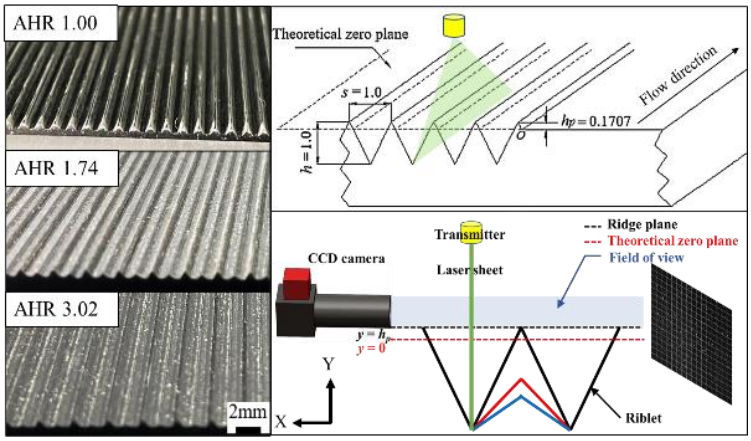

b) Experimental model and shooting position

Fig. 2. Schematic of experimental system.

Table 2 Size of the wind tunnel

mm	Feature	Chamber	Contraction	Test	Diffuser
L	3000	320	320	850	1250
W	350	350	350	350	350
H	—	300	—	85	—

The particle generator driven by the air compressor forms olive oil droplets (diameter: 1 μm) as tracer particles that are uniformly distributed in the flow field. During this study, the Dantec PIV system is used to measure two components of velocity with tracer particles dispersed in the airflow. A laser light sheet with a thickness of approximately 1 mm generated by a Litron double cavity Nd-YAG laser (Energy: 2×30 mJ, wavelength: 532 nm, time delay 500 μs) is used as the excitation light; a CCD camera (HiSense MKII, Dantec Dynamics) can capture the flow in the (*x*-*y*)-plane near the wall. The test section has a rectangular cross section of 46×320 mm^2 and a length of 850 mm. The test plate has the same length as the test section. The shooting position is set to 65δ in the streamwise direction to provide a fully developed turbulent flow at the field of the CCD camera. The variable δ denotes the channel half-height, which is 23 mm in this case. The CCD camera records two images of the tracer particles per unit time when laser excites these tracer particles during the experiment. The synchronization of the camera and laser light sheet was controlled via Dantec Dynamic Studio software. A total of 2000 pairs of images were recorded for each operating condition from the visual field by the CCD camera (resolution: 2048×2048 pixels, sampling frequency: 70 Hz, the pulse interval: 10 μs) to obtain the information from the flow field by processing the time interval between two images of the particle in the window. The displacement of the tracer particles is 8–10 pixels between two images for a vector field to satisfy the precision demand for PIV. The PIV processing resulted in a final interrogation area of 32 × 32 pixels with 75% overlap to acquire the information of the flow field. QM 100 long-distance microscope (30003, Questar) with smaller field of view (FOV: 3×3mm) is connected to the CCD camera to record the images of flow to avoid the reflection of walls, which affects the near wall experimental flow field. The streamwise velocities of 7, 8, and 9 m/s were experimented in four geometry cases, including three types of riblet shapes and a smooth surface. The corresponding Reynolds numbers (Re_L) are 4.07×10^5, 4.66×10^5, and 5.24×10^5 during the experiment.

$$\mathrm{Re}_L = \frac{\rho u L}{\mu} \tag{4}$$

where ρ and μ are density and dynamic viscosity of air, respectively, u is free-stream velocity, and L is the feature-length of the test section, which is 850 mm in this experiment.

2.3 Numerical Model Validation

The enhanced wall function in the turbulence model should ensure that the y^+ value of the first node of the near-wall unit is close to 1 (see Fig. 1c). Thus, the required refinement of the near-wall unit is closely related to the free stream velocity (as shown in the inset of Fig. 3(a)). The height of the first layer of the unit should be approximately 0.032 mm

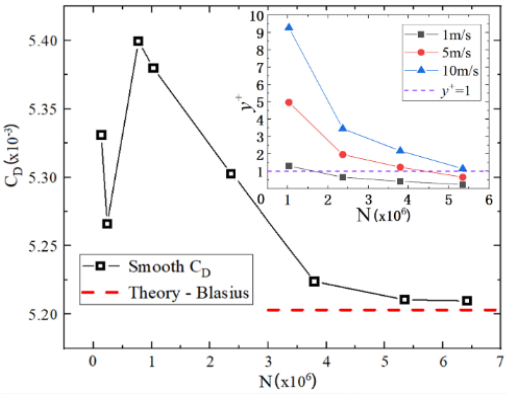

(a) Mesh refinement and independence verification

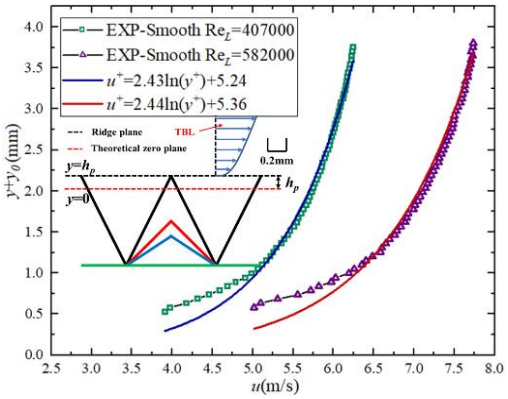

(b) Log-law plot of mean velocity experiment profiles over smooth plates at 10 m/s

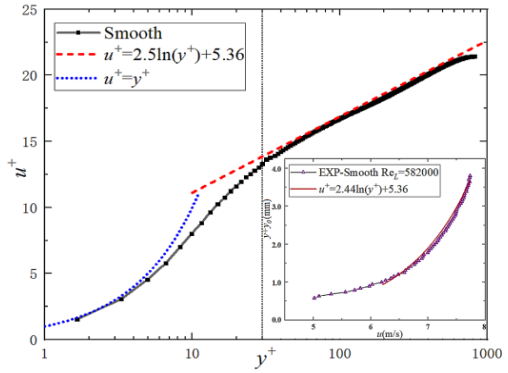

(c) Log-law plot of mean velocity numerical simulation profiles over smooth plates at 10 m/s

Fig. 3. Verification of simulation and experiment.

(corresponding to 6.42 million elements). The drag coefficients C_D of the smooth surface from the numerical results are compared with the theoretical solution of equation (5) to satisfy the requirements of the model at the velocity of 10 m/s (corresponding to Re_L=5.82×10^5). The drag coefficient of the TBL on the plate is defined as follows:

$$C_D = \frac{0.074}{\sqrt[5]{\mathrm{Re}_L}} \tag{5}$$

Thus, the target Blasius theoretical solution shown in Fig. 3 (dotted red line) is 5.203×10^{-3}.

Results show that increasing the number of elements in the finite volume model (FVM) from 5.35 million to 6.42 million changes the drag coefficient by only 0.15%. Thus, using the 5.35 million elements provides sufficient resolution for the simulations, as shown in Fig. 3(a). In terms of PIV experiment, the fitting work of the log-law curve should be conducted for each different shaped riblet to measure κ and B for a smooth surface based on experimental results. Lastly, the friction velocity u_τ under different working conditions can be obtained. The expression of smooth plates under log-law region is as follows:

$$u^+ = \frac{1}{\kappa}\ln y^+ + B \tag{6}$$

$$f = \lg(y^+) - \lg\left\{\exp\left[\kappa(u^+ - B)\right]\right\} = 0 \tag{7}$$

where κ indicates the von Kármán constant, and B is the constant for a smooth surface based on the experimental results. Equation (6) is used to nondimensionalize the distance y and the free-stream velocity (Qiu *et al.* 2020) u to obtain the wall variable y^+ ($y^+=(y+y_0)u_\tau/\nu$) and u^+ ($u^+=u/u_\tau$) (as shown in Fig. 3(c)). The expression of the wall friction velocity is as follows:

$$u_\tau = \left(\frac{\tau_w}{\rho}\right)^{\frac{1}{2}} \tag{8}$$

where τ_w indicates the magnitude of the shear stress at the wall, and ρ is the air density.

The velocity field of the position of the CCD camera field of view during the PIV experiment should be revised because the theoretical zero point of the riblet wall is lower than the ridge plane. According to the research of Bechert *et al.* (1997), a virtual origin is observed near the V-groove riblet, and its distance from the tips of the ridges is called the protrusion height $h_p=y_0$. Therefore, the dimensionless normal height y^+ can be derived by the sum of the normal height y and the h_p in the camera field of view, as shown in Fig. 3(b). The calculation formula of h_p on the V-groove riblets (Yan *et al.* 2021) is as follows:

$$\frac{h_p}{s} = \frac{1}{2\pi}\left[\gamma + 2\ln 2 + \frac{\pi}{\tan\alpha} - \frac{\pi}{\alpha} + \psi\left(1+\frac{\alpha}{\pi}\right)\right] \tag{9}$$

where s is the rib spacing, γ = 0.5772 is the Euler constant, and ψ is the Digamma function. (Bechert *et al.* 1997)

For the convenience of discussion, the near-wall velocity profiles are obtained from the ridge plane, where the opening angle α of the riblet is 60° to calculate the relation of h_p and s (s=1 mm) as $y_0=h_p$=0.1707×s. Therefore, h_p is 0.1707 mm. During the PIV experiment, as shown in Fig. 3(b), we regard κ, B, and u_τ as unknown variables, apply the nonlinear curve fitting to the imported experimental measurement data u-y, and solve the minimum of the over-constrained equation (4) f (κ, B, u_τ) =0 in the entire time domain quadratic solution (Clauser 1954; Kendall and Koochesfahani 2007). The experimental fitting curve in Fig. 3(b) shows that the constants B of the two inflow velocities are 5.24 and 5.36. In addition, their von Karman constant is approximately 0.41. The log-law distribution line obtained by the simulation in Fig. 3(c) indicates that the constant B of the experiment and simulation at the same Re_L=5.82×10^5 is 5.36, confirming the accuracy of the simulation. In addition, the velocity profile of a smooth surface fits the linear distribution of the viscous sublayer under y^+＜5, which is also nearly coincident with the log-law of equation (6) when y^+ ＞30(Choi 2006). These results prove that the free-stream velocity near the wall at the area captured by the CCD camera reaches the fully developed turbulence. These conditions ensure the feasibility and accuracy of the simulation method.

3. DISCUSSION OF RESULTS

3.1 Effect of V-groove Riblets on Time-Averaged Velocity Distribution Near the Wall

As shown in Figs. 4 a–c, extracting the velocity curves of a smooth surface and different AHR riblets at the central axis in the camera field of view after revising y^+ is essential. The wall friction velocity u_τ must be determined prior to calculating the drag reduction rate because the effect of the turbulence should be measured. However, this value is difficult to obtain accurately during the experiment. Curve fitting is performed using the least square method (Wang *et al.* 2021) in the experiments to obtain the friction velocity u_τ of different riblets indirectly under other working conditions, according to the above model validation method. Thus, the drag reduction effect of the TBL can be further analyzed. Figures 4(a–b) show the time-averaged velocity profiles at Re_L of 4.07×10^5 and 5.24×10^5 (The EXP. data are obtained from the red centerline of the camera field of view in the lower right corner of Figs. 4-a and b). The comparison of the two figures indicates that the velocity curves of V-groove riblets under different AHRs in the log-law region (30< y^+<100) decrease with the increase in flow velocity and approach gradually the velocity curve of a smooth surface.

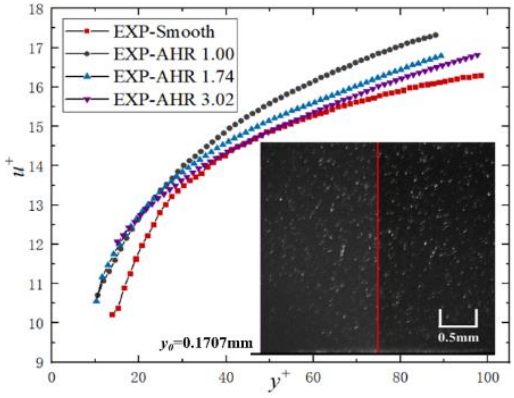

(a) 7 m/s velocity profile

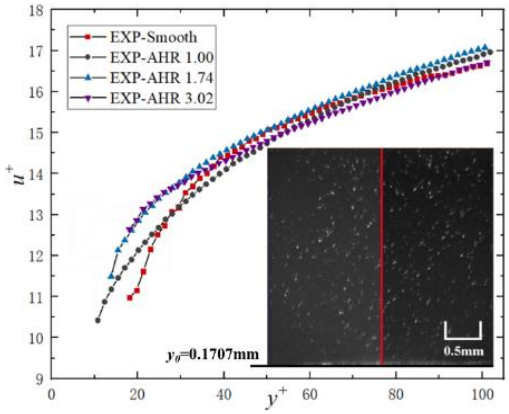

(b) 9 m/s velocity profile

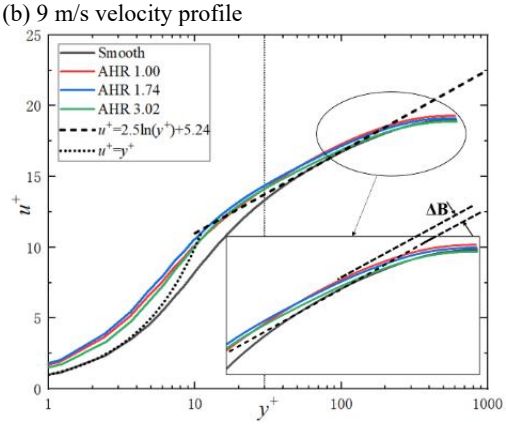

(c) CFD simulation at 7 m/s

Fig. 4. Mean velocity profile of the TBL over the smooth and different AHR riblet plates.

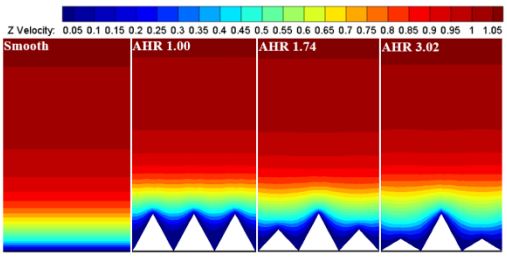

Fig. 5. Velocity contour of smooth plates and riblets with different AHRs.

This finding indicates that the drag reduction effect of the three types of riblets near the wall decreases when the free-stream velocity is high. In addition, an upward shift (ΔB) (Zhang *et al.* 2020b) of the logarithmic velocity profile evidently indicates that the thickness of the viscous sublayer is increased, as a result of turbulent drag reduction due to the V-groove riblets (Fig. 4c). Moreover, the lift-up effect (Choi 2006) of the AHR=1 riblets is better than that of the other V-groove riblets (AHR = 1.74, 3.02), indicating that the AHR=1 has better drag reduction effect.

Figure 4 shows that the free-stream velocity near the wall is affected by different geometrical shapes of the riblets. Different from the transverse riblets, the PIV experiment of the longitudinal riblets cannot capture the distribution of internal flow field below the ridge plane due to the limitations of shooting angle and model placement. The tracer particles used in the experiment are led into the wind tunnel from the top side of the chamber section. Under a low velocity (such as 1 m/s), obtaining a stable flow field image is difficult because the following behavior of the tracer particle in the flow field cannot be driven fully by the airflow in the test section. Therefore, the flow velocity distribution contours in the V-groove riblets should be extracted by simulations. Figure 5 shows the velocity contour of smooth plates and riblets with different AHRs at z=25 mm (midplane x-y) when the free-stream velocity is 1 m/s. The thickness of the blue low-velocity region (indicated by the white dividing line), where the streamwise velocity of the V-groove riblet is between 0 and 0.05 m/s, is larger than that of the smooth plate, and the area of this region decreases with the increase in the adjacent height ratio. This effect of riblets also reveals that the existence of the riblet shape increases the thickness of the viscous sublayer and reduces the direct influence of the high-speed fluid in the wake region on the solid wall, thereby reducing the flow resistance. It confirms the experimental result obtained by previous studies (Qiu *et al.* 2020; Modesti *et al.* 2021; Zhang *et al.* 2020a), that is, the viscous sublayer of the TBL on the wall of the V-groove riblet is thicker than that of the smooth plate. Moreover, increasing the AHR of the riblets results in a larger region of flow retardation inside the grooves.

3.2 Effect of Riblet Structure on Wall Shear Stress and Drag Reduction Rate

The drag reduction can be quantified as the difference in the skin friction coefficients between the smooth plate and the V-groove riblet. It is simply and qualitatively analyzed in the above-mentioned near-wall velocity profiles. The wall friction velocity u_τ is vital to further investigate the quantitative drag reduction rate η of various walls on the airflow. First, u_τ under different Re_L obtained by the fitting method is used to deduce (Equation 7) the time-averaged wall shear stress τ_w near the wall of the TBL. Second, the mean skin friction coefficients C_f can be calculated by Equation 10. Finally, the drag reduction rates of the V-groove riblets can be calculated according to Equation 11, and the specific data are shown in Table 3.

Table 3 Parameters and drag reduction rate of TBL on smooth plate and riblet plates under different Re_L.

surface	Re_L	u_τ	τ_w	$C_f\times10^{-3}$	η
AHR 1.00	4.07×10^5 5.24×10^5	0.369 0.441	0.1668 0.2382	5.5576 4.8020	3.655% 3.501%
AHR 1.74	4.07×10^5 5.24×10^5	0.370 0.443	0.1677 0.2404	5.5876 4.8457	3.394% 3.063%
AHR 3.02	4.07×10^5 5.24×10^5	0.374 0.448	0.1713 0.2459	5.7092 4.9557	2.350% 1.969%
Smooth	4.07×10^5 5.24×10^5	0.383 0.457	0.1797 0.2558	5.9873 5.1568	— —

The mean skin friction coefficient C_f can be defined as follows:

$$C_f = \frac{\tau_w}{\left(\frac{\rho u_\infty^2}{2}\right)} = 2\left(\frac{u_\tau}{u_\infty}\right)^2 \tag{10}$$

The drag reduction rate η is obtained as follows:

$$\eta = \frac{C_{fs} - C_{fg}}{C_{fs}} \times 100\% \tag{11}$$

where u_∞ indicates the free-stream velocity, C_{fs} and C_{fg} represent the skin friction coefficients of smooth surface and riblet-textured surface, respectively.

The wind tunnel PIV experimental data are shown in Table 3. When $Re_L=4.07\times10^5$, the drag reduction rate of the V-groove riblet with AHR=1 is 3.655%. In addition, when $Re_L=5.24\times10^5$, the rate of drag reduction decreased to 3.501%, indicating that the drag reduction rate of the groove wall decreased with the increase in the free-stream velocity. Moreover, the drag reduction rate of V-groove with two other AHRs has the same trend, further confirming that this conclusion is consistent with that of Bai *et al.* (2016b). Constrained by the size of the test section, the CCD camera cannot obtain the stable flow field near the wall at low flow velocity. Thus, whether the drag reduction rate decreases with the increase in flow velocity under other flow velocity conditions should be validated. Therefore, the drag reduction rate of V-groove with AHR = 1 is higher than that of V-groove riblets (AHR = 1.74, AHR = 3.02) after analyzing the drag reduction rates of the three riblet structures by using the time-averaged near-wall velocity curve calculated by simulation in Fig. 6. It also proves the conclusion of drag reduction rate obtained by fitting the near-wall velocity curve under the experimental photographing condition. After determining the drag reduction rate, the drag reduction principle of different AHR riblet structures should be explored in depth. The wall viscous friction drag of channel flow is the result of the integration of the wall shear stress to the area, but the magnitude of the shear stress distribution at the wall below the riblet ridge plane cannot be captured due to the objective factor of the photographic view of CCD camera during the PIV experiment. However, the magnitude of the shear stress at the wall directly affects the surface viscous friction drag. Thus, extracting the wall shear stress profiles of the V-groove riblets in the calculation domain by simulation is crucial (Fig. 7).

The inset of Fig. 7 shows the V-groove shapes, with colors corresponding to the wall shear stress (WSS) of the riblets at different AHRs. The WSS at the tip of the three V-groove riblets is the largest at 0.43, 0.50, and 0.37 Pa for the plates with AHRs of 1.00, 1.74, and 3.02, respectively. The minimum value of the WSS tends to present at the valley of the trough; this value decreases rapidly along the V-groove wall from the tip to the bottom. With the increase in AHR, the minimum WSS increases gradually,

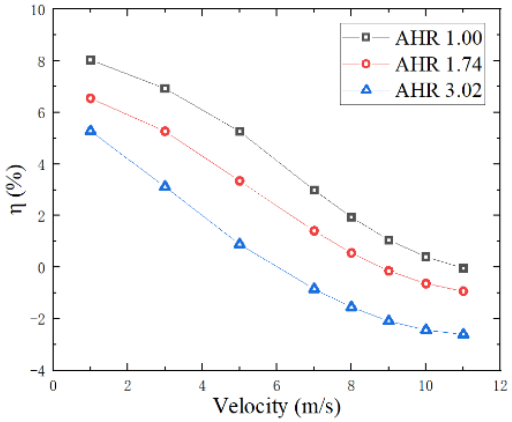

Fig. 6. Mean velocity distribution at different Reynolds numbers.

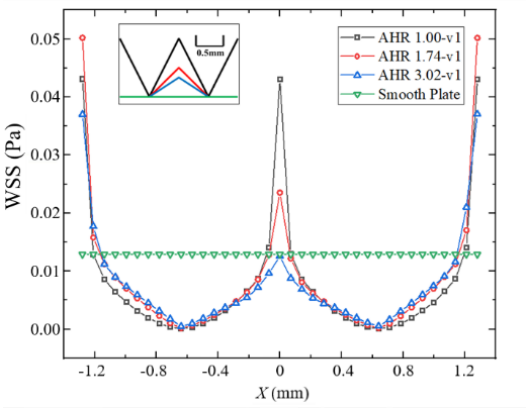

Fig. 7. Curves of wall shear stress of smooth and riblet surfaces at u=1 m/s.

corresponding to 0.001, 0.0023, and 0.0031 Pa. The mean WSS of the smooth surface is 0.01293 Pa, and 0.01189, 0.01208, and 0.01225 Pa for riblets with the AHRs of 1.00, 1.74, and 3.02, respectively; these values are smaller than the WSS of the smooth plate. This result demonstrated that the V-groove shapes can play a role in reducing the frictional drag of the wall.

3.3 Effect of Riblet Structure on Pulsation Characteristics

The PIV experiments are used to analyze the pulsation characteristics of riblets and smooth in this section because collecting accurate fluctuating velocity data by common CFD transient calculation is inconvenient. Turbulent intensity is a crucial physical quantity to measure the intensity of turbulent fluctuation, which reflects the fluctuation of fluid flow. Figure 8 shows the curves of the turbulent intensity and Reynolds shear stress (RSS) distributions in the wall-normal direction near the riblet and smooth surface when Re_L=4.07×10^5 during the PIV experiment. Figures 8(a) and (b) show that when in the log-law region ($30 < y^+ < 100$), the streamwise turbulent intensity $\sqrt{\overline{u'^2}}/U_e$ and the wall-normal turbulent intensity $\sqrt{\overline{v'^2}}/U_e$ on the V-groove riblet are significantly smaller than those of the smooth plate. Meanwhile, the turbulent intensity of different V-groove shapes is unremarkably different from each other, where u' and v' represent the streamwise and wall-normal fluctuating velocity, respectively. Moreover, U_e represents the time-averaged velocity at a specific location of the CCD camera field of view. These results show that the existence of the V-groove riblet reduces the velocity pulsation in the streamwise and the wall-normal direction, causing the streamwise flow in the near-wall region to become relatively stable to further reduce the intensity of turbulent transport. In addition, considering the groove with AHR=3.02, the peak value of the wall-normal turbulent intensity (0.075) in the log-law region is significantly smaller than that of the streamwise turbulent intensity (0.160), further indicating that the V-groove riblets mainly weaken the streamwise turbulence near the wall, but slightly affect the wall-normal turbulent pulsation.

The RSS $-R\langle u',v'\rangle$ curve (Fig. 8c) along the wall-normal shows that the RSS of the V-groove riblet near the wall is significantly smaller than that of the smooth surface in the buffer layer and logarithmic layer, and the maximum difference is approximately 30%. Evidently, the groove wall restricts the pulsation of the streamwise vortex associated with the low-speed strip in the near-wall region, causing the near-wall flow of the V-groove riblets to become more stable, thereby enhancing the drag-reducing effect (Zhang *et al.* 2020a). The velocity pulsation phenomenon of the V-groove riblets with the AHR=1 is smaller than that of other AHR riblets in terms of the turbulent intensity and RSS distribution near the wall slightly. Thus, the form of coherent vortices along the streamwise is reduced to obtain better drag reduction characteristics.

Vorticity is an important variable to measure the stability of flow, which is mainly reflected in the curl of the velocity field. Thus, various V-groove shapes should be used to explore the influence law of the vorticity. In this section, CFD simulation is used to study the vorticity intensity of different V-groove riblets to further determine the effects of the V-shape trenches with different AHRs on the turbulent flow characteristics, and the total vorticity $|w|$ is defined for this purpose.

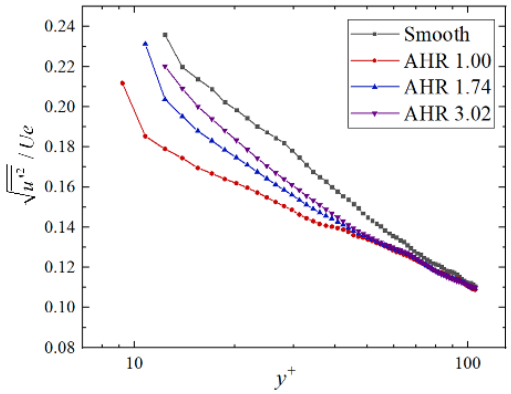

a) Distribution of the streamwise turbulent intensity

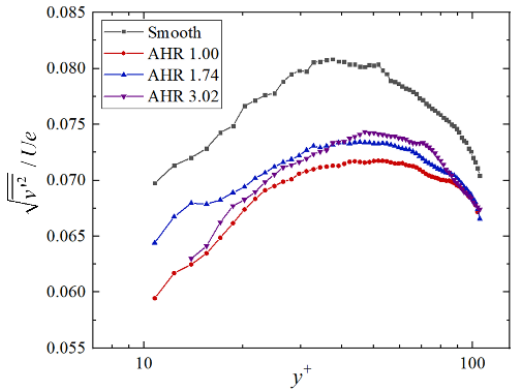

b) Distribution of the wall-normal turbulent intensity

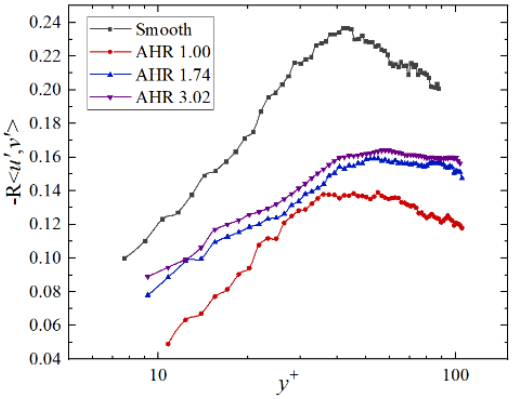

c) Distribution of the RSS

Fig. 8. Turbulent intensity and RSS distributions in wall-normal direction.

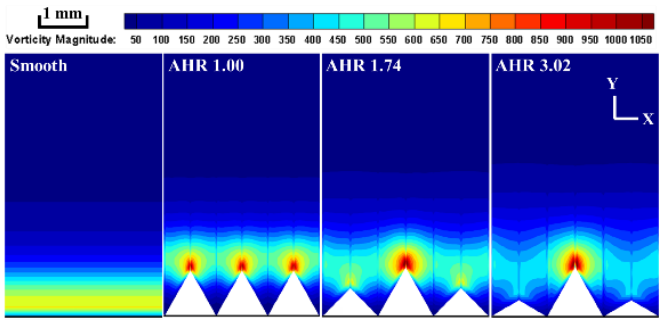

Fig. 9. Vorticity plots of groove surfaces at AHRs.

$$\vec{w} = \vec{\nabla} \times \vec{u}$$
$$w_x = \frac{\partial u_z}{\partial y} - \frac{\partial u_y}{\partial z}, w_y = \frac{\partial u_x}{\partial z} - \frac{\partial u_z}{\partial x}, w_z = \frac{\partial u_y}{\partial x} - \frac{\partial u_x}{\partial y} \quad (12)$$
$$|w| = \sqrt{w_x^2 + w_y^2 + w_z^2}$$

where w_x, w_y, and w_z represent vorticity values in three directions.

Figure 9 shows the total vorticity $|w|$ contour plot of the smooth plate and the different AHR riblets at Z=25 mm ((x-y)-plane). Compared with the smooth plate, more high-intensity vorticity regions are gathered near the opening angle α of the V-groove riblets (Ng *et al.* 2018; Raayai–Ardakani and McKinley 2019). The total vorticity, as a representation of the fluid curl, can show the strong shear effect of the near-wall flow vortex on the opening angle of the riblets, objectively, whereas weak flow vortices are concentrated at the valley of the troughs. This finding indicates that the V-grooves may play a key role in breaking up the streamwise vortices to weaken the shearing effect of the fluid near the wall. Moreover, the structural characteristics of the V-groove riblets prevent the high WSS near the opening angles from reaching the viscous region of the valley of troughs. The result is similar to the finding obtained from the WSS curves of different groove surfaces in Section 2.2. The contact area of exposure between the groove and the airflow under higher time-averaged WSS condition can be reduced for the purpose of drag-reducing effect (Yan *et al.* 2021). In addition, for the grooves with AHR=1.00, the peak value of vorticity ($|w_1|_{max}$=1094 s^{-1}) is smaller than that of the non-equal height riblets as indicated by the vorticity pattern of the riblets with different AHRs. The values of the two other riblets are $|w_2|_{max}$=1250s^{-1} and $|w_3|_{max}$=1284s^{-1}. This result proves that the increase in the AHR leads to the enhancement of the peak value of the total vorticity. Thus, the secondary flow over riblets is sufficiently strong to transport momentum in the near-wall region. A generally accepted conclusion is that the larger vorticity results in greater vortex effect on the near wall velocity (Li and Liu 2019). Thus, the riblets of the bionic non-equal height enhance the probability and range of action about the magnitude of vorticity, whose results are consistent with the findings of Modesti *et al.* (2021) and Qiu *et al.* (2020). For the turbulent flow over the riblets, the secondary flow motion is passively generated, owing to the streamwise-parallel setting of the riblets and the inherent cross-flow motions of a turbulent boundary layer. Therefore, the generation of the cross stream secondary flow motion does not explain the net drag reduction (Suzuki and Kasagi 1994).

3.4 Effect of V-groove Riblets on the Coherent Structures of Turbulence

Recent surveys (Chavarin and Luhar 2020; Li *et al.* 2021,; Modesti and Endrikat 2021) show large-scale coherent motions near the wall at high Reynolds numbers, significantly causing the formation of skin-friction drag. At present, a widely recognized finding is that the turbulent motions undergo a rapid cycle of events culminating in their eruption from the wall region, known as "bursting." Usually, "ejection" (Q2: $u' < 0$, $v' > 0$) and "sweep" (Q4: $u' > 0$, $v' < 0$) events tend to be analyzed as a fundamental method on turbulent coherent structures for drag reduction because the Q2 and Q4 events greatly affect the frictional resistance of the wall region (El-Samni *et al.* 2007). As summarized by Abreu *et al.* (2020), the "bursting" process composed of the "sweep" of high-speed fluid and the "ejection" of low-speed fluid is the source of near-wall Reynolds shear stress. Thus, the ideal AHRs for V-groove riblets should avoid unexpected drag and turbulent diffusion by investigating Q2 and Q4 events. The peak value of the Reynolds stress of the V-groove riblet appears at the position near y^+=50 from the distribution curve of Reynolds shear stress. We extracted the 2D topologies of the pulsation velocities of the Q2 and Q4 events near the y^+=50 region at Re_L=4.07×10^5 from the different AHR riblets to further analyze the influence of the coherent structures on the flow patterns. Based on the improved quadrant splitting method (ISQM), 2000 sheets of the turbulent coherent structures with a free-stream velocity of 7 m/s were sampled in the riblets with different AHRs.

$$\begin{aligned} Q_2 &= 1(\text{ejection}), \text{if } u'v' > H_0\left|\overline{u'v'}\right| \& u' < 0 \& v' > 0 \\ Q_4 &= -1(\text{sweep}), \text{if } u'v' > H_0\left|\overline{u'v'}\right| \& u' > 0 \& v' < 0 \\ 0, &\quad \text{otherwise} \end{aligned} \quad (13)$$

where H_0=1.0 represents the threshold. Equation (13) reflects the motion of fluid during ejection and sweep.

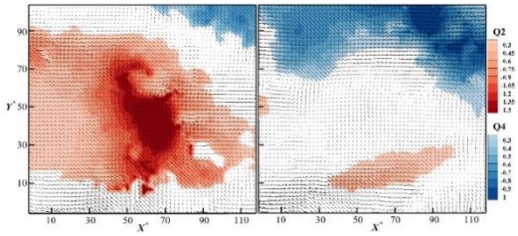

(a) Distribution of Q2 and Q4 events on smooth plate

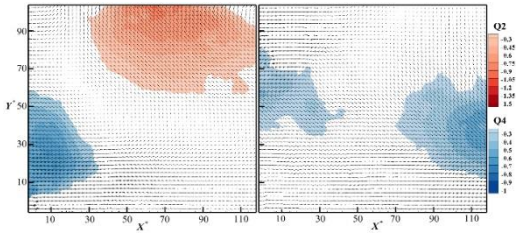

(b) Distribution of Q2 and Q4 events on AHR=1.00

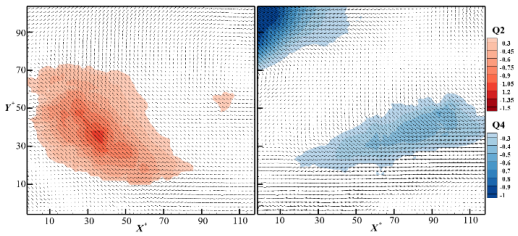

(c) Distribution of Q2 and Q4 events on AHR=1.74

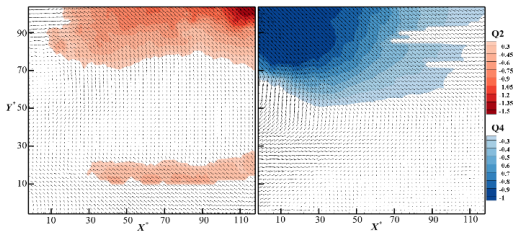

(d) Distribution of Q2 and Q4 events on AHR=3.02

Fig. 10. Distribution of Q2 & Q4 events on different near-wall surfaces.

Figures 10(a–c) show the distribution of coherent events ((*x*-*y*)-plane) of the riblets with different AHRs at Re_L=4.07×10^5 during the PIV experiment. The red regions in the left contour plots represent the 2D topologies of the pulsating velocity when the low-velocity fluid near the different riblets is brought up to the outer part of the boundary layer by the Q2 event. However, the blue regions in the right contour plots represent the 2D topologies of the pulsating velocity when the high-velocity fluid in the outer flow is brought down to the wall by the Q4 event. All the abscissas and ordinates in Fig. 10 are dimensionless by the wall friction velocity u_τ to obtain the dimensionless X^+ and Y^+.

For the convenience of discussion, the threshold for the occurrence of bursting events is defined as 0.25 times the maximum value of the fluctuating velocity (Wang *et al.* 2022), and the 2D distribution pattern of the turbulent coherent structures along the flow direction is extracted based on this setting. Figure 10 shows that the area of the bursting event (including Q2 and Q4 events) for the V-groove riblets with AHR=1.00 is significantly smaller than that of the AHR=3.02 and the smooth plate. In addition, in terms of the riblet with AHR=1.00, the peak values of the fluctuating velocity of the Q2 event and the Q4 event are −1.0 and −0.7, respectively, which are much smaller than those of the riblets with AHR=1.73 ($Q2_{peak}$ = -1.2, $Q4_{peak}$ = −1.3) and the riblets with AHR=3.02 ($Q2_{peak}$ = −1.6, $Q4_{peak}$ = −1.4). Moreover, the riblets with the three structures are significantly smaller than smooth plate in terms of bursting event intensity ($Q2_{peak}$ = −1.9, $Q4_{peak}$ = -1.5). The V-shaped riblets of equal height reduce the velocity difference between the low-velocity fluid rising due to the Q2 event and the surrounding fluid, which is more conducive to suppressing the intensity of the Q2 and Q4 events of the turbulent coherent structures. Moreover, with the increase in AHR, the intensity of the bursting events becomes more intense by comparing the non-equal-height riblets. This condition causes not only more high-velocity airflows to be brought from the central area to the wall by the Q4 event, but also more low-speed gas from the wall to the central high-speed area by the Q2 event in the test section, greatly hindering the drag reduction effect.

The joint probability density function (JPDF: P(*u'*, *v'*)) of various surfaces was obtained using Matlab to conduct a detailed quadrant analysis of the Reynolds shear stress covariance of various near-wall structures in a turbulent channel flow with Re_L=4.07×10^5 (Ong and Wallace 1998).

$$\overline{u'v'} = \iint_{-\infty}^{+\infty} u'v'P(u',v')\mathrm{d}u'\mathrm{d}v' \tag{14}$$

where the integral of the covariance integrand, *u'v'*P(*u'*, *v'*), over a differential area d*u'*d*v'* of the (*x*-*y*)-plane (Perry and Hoffmann 1976) represents the contribution of that particular simultaneous combination of sign and magnitude of *u'* and *v'* to the Reynolds shear stress covariance.

Plots of P(*u'*, *v'*) and *u'v'* P(*u'*,*v'*) for the present boundary layer experiment are shown in Fig. 11 for y^+ =50. Figure 11(a) denotes the JPDF distributions of *u'* and *v'* for different wall structures within the field of view captured by the CCD camera. Clearly, at low values of Re_L, the distribution areas of Q2 and Q4 events for the different near-wall surfaces are significantly larger than those of Q1 and Q3 event regions, confirming that the turbulent wall friction is increased because bursting is one of the main sources for its production. Moreover, the JPDF on the three types of V-groove riblets is more concentrated in the Q2 and Q4 event distribution areas than that of smooth wall, indicating that the occurrence probability and the intensity of the larger fluctuating velocity are significantly smaller than those of the smooth wall. The result further reflects that the riblets could hamper the near-wall momentum exchange and delay the development of initial turbulent structures. As shown in Fig. 11(b), the distribution area of Q2 event is the largest among the four surface shapes, especially the Q2 events of the flat plate, whose maximum fluctuating velocity can reach 2.2 m/s. The distribution ranges of Q1 and Q3

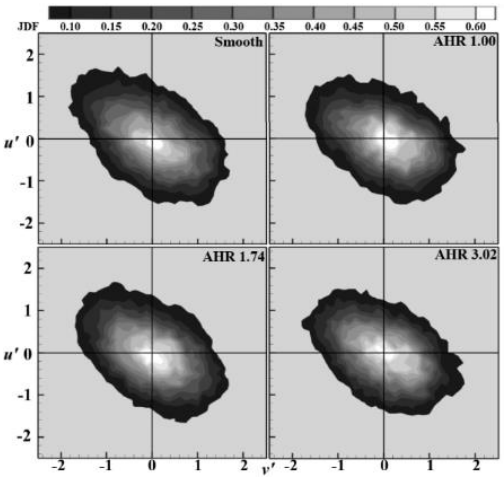

(a) Joint probability distribution function, P(*u'*, *v'*)

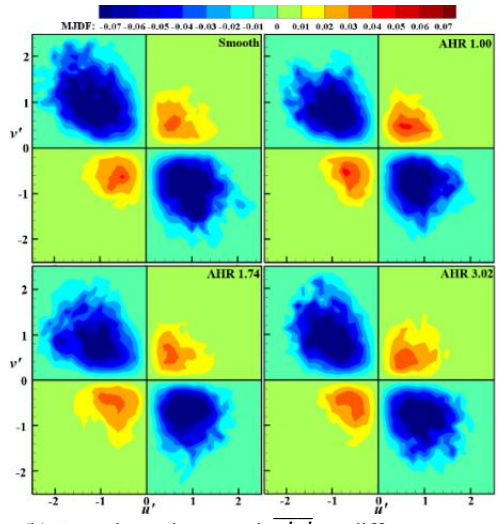

(b) Covariance integrand, $\overline{u'v'}$ on different near-wall surfaces.

Fig. 11 Joint probability density distribution of the bursting events on different near-wall surfaces at $y^+ = 50$ in a turbulent channel flow with $Re_L=4.07\times10^5$

events of the three riblet structures are compared, and the results show that the riblet with AHR=1 has the most concentrated distribution pattern near the origin (*u'*=*v'*=0), thereby revealing that the AHR=1 structure is better than the other non-equal height riblet in restraining the magnitude of turbulent bursting events. In summary, the riblet with AHR=1 has the best drag reduction effect.

4. CONCLUSION

This study investigates the effect of the V-groove riblets with different AHRs on the time-averaged velocity distribution near the wall from the particle image velocimetry (PIV) experiment and calculates the drag reduction rate. The above calculation results are combined with the numerical simulation to obtain the wall shear stress distribution of riblets with different shapes and the profiles of drag reduction rate under different flow patterns. The influence of the turbulence intensity, the Reynolds stress, and the turbulent coherent structures on the drag reduction effect was further analyzed by extracting the fluctuating velocity profiles near the wall. Finally, the V-groove shape with the best drag reduction was determined. Based on the measured boundary layer profiles, the following conclusions with regard to turbulence statistics and the validity of the proposed method evaluating the reduction of skin friction drag were drawn as follows:

(1) In terms of V-shaped riblets with different AHRs, the wall friction velocity is less than that of the smooth plate, and the log-law layer of the mean velocity profile moves outward significantly compared with that of the smooth plate. This phenomenon increases the thickness of the TBL, reduces the time-averaged velocity gradient on the wall, and further reduces the surface friction resistance. In addition, the V-groove riblet with AHR=1 has thicker viscous sublayer and smaller velocity gradient than the groove with other height ratio; thus, it has the best drag reduction effect.

(2) The V-groove riblets have a positive drag-reducing ability in a certain velocity range. Moreover, one interesting finding is that the drag reduction rate decreases with the increase in two factors (adjacent height ratio and free-stream velocity). The maximum drag reduction can reach up to 8.03% when the adjacent height ratio is 1:1 and the velocity is 1 m/s.

(3) The V-shaped riblets with AHR=1 have significantly smaller streamwise and wall-normal turbulent intensity than other riblet structures near the wall in the region of $y^+<100$, indicating that the riblet structure mainly weakens the turbulence pulsation intensity of the flow direction; therefore, the streamwise flow near the wall is relatively stable. Moreover, the riblet with non-equal heights forms a stronger secondary flow because the vorticity patterns inside the riblets obtained by the CFD simulation result in greater frictional drag.

(4) Compared with the two other non-equal height riblet structures, the riblets with AHR=1 significantly suppresses the ejection (Q2) event and the sweep (Q4) event during the "bursting" of the coherent structures of the TBLs, reduces the streamwise and fluctuating velocity in the process of the Q2 and Q4 events, inhibits the energy exchange of the turbulent fluid, and thus plays the role of drag reduction.

ACKNOWLEDGEMENTS

The authors would like to thank Prof. Zhang Hua of Beihang University for his excellent technical support during the setup of our experimental rig. They also would like to acknowledge the timely technical advice provided by Prof. Jiang Nan and Prof. Tang Zhanqi at Tianjin University.

Competing Interests

All authors disclosed no relevant relationships.

Authors' Contributions

Z. M. Liu, R. Chen and Q. Tian wrote the main manuscript text; Z. M. Liu and Y. Pang reviewed the manuscript; Z. Q. Tang provided suggestions and guidance for the experiment and simulation, and review the article; the PIV experiment was conducted by R. Chen, Y. C. Fang, P. J. Li, and L. Li.

Funding

The authors wish to thank the support of the National Natural Science Foundation of China (12172017, 11872083 and 11702007) and the Aviation Science Foundation of China (No. 20150375001， No. 20160375001).

Availability of Data and Materials

All data generated or analyzed during this study are included in this published article.

REFERENCES

Abreu, L. I., A. V. G. Cavalieri, P. Schlatter, R. Vinuesa and D. S. Henningson (2020) Resolvent modeling of near-wall coherent structures in turbulent channel flow. *International Journal of Heat and Fluid Flow* 85.

Launder, B. E. and D. B. Spalding (1972). *Lectures in Mathematical Models of Turbulence*. Academic Press, London, England.

Bai, X., X. Zhang and C. Yuan (2016a). Numerical analysis of drag reduction performance of different shaped riblet surfaces. *Marine Technology Society Journal* 50, 62-72 .

Bai, Q., J. Bai, X. Meng, C. Ji and Y. Liang (2016b). Drag reduction characteristics and flow field analysis of textured surface. *Friction* 4, 165-175.

Bechert, D. W, M. Bartenwerfer (1989). The viscous flow on surfaces with longitudinal ribs. *Journal of Fluid Mechanics* 206, 105-129.

Bechert, D. W., M. Bruse, J. Hoeven, W. Hage and G. Hoppe (1997). Experiments on drag-reducing surfaces and their optimization with an adjustable geometry. *Journal of Fluid Mechanics* 338, 59-87.

Boomsma, A. and F. Sotiropoulos (2016). Direct numerical simulation of shark skin denticles in turbulent channel flow. *Physics of Fluids* 28, 035106.

Chavarin, A. and M. Luhar (2020). Resolvent analysis for turbulent channel flow with riblets. *AIAA Journal* 58, 589-599.

Chen, H., C. Pan and J. Wang (2013). Effects of sinusoidal leading edge on delta wing

mounted surfaces. *Acta Mechanica Sinica* 35, 457-471.

performance and mechanism. *Science China Technological Sciences* 56, 772-779.

Chen, H., F. Rao, X. Shang, D. Zhang and I. Hagiwara (2014). Flow over bio-inspired 3D herringbone wall riblets. *Experiments in Fluids* 55, 1698-1705.

Choi, K. S. (2006). Near-wall structure of a turbulent boundary layer with riblets. *Journal of Fluid Mechanics* 208, 417-458.

Clauser, F. H. (1954) Turbulent boundary layers in adverse pressure gradients. *Journal of the Aeronautical Sciences* 21, 91-108.

El-Samni, O. A., H. H. Chun and H. S. Yoon (2007). Drag reduction of turbulent flow over thin rectangular riblets. *International Journal of Engineering Science* 45, 436-454.

Fang, F. M., J. C, Chen and Y. T. Hong (2001). Experimental and analytical evaluation of flow in a square-to-square wind tunnel contraction. *Journal of Wind Engineering and Industrial Aerodynamics* 89, 247-262.

Feng, B., D. Chen, J. Wang and X. Yang (2015). Bionic research on bird feather for drag reduction. *Advances in Mechanical Engineering* 7, 1-10.

Heidarian, A., H. Ghassemi and P. Liu (2018). Numerical analysis of the effects of riblets on drag reduction of a flat plate. *Journal of Applied Fluid Mechanics* 11, 679-688.

Walsh, M. J. (1980). Drag characteristics of V-Groove and transverse curvature riblets viscous flow drag reduction. *AIAA journals*168-184.

Jung, Y. C. and B. Bhushan (2010). Biomimetic structures for fluid drag reduction in laminar and turbulent flows. Journal of Physics: Condensed Matter 22, 035104.

Joshi, K. and S. Bhattacharya (2019). Large-eddy simulation of the effect of distributed plasma forcing on the wake of a circular cylinder. *Computers & Fluids* 193, 104295.

Kendall, A. and M. Koochesfahani (2007). A method for estimating wall friction in turbulent wall-bounded flows. *Experiments in Fluids* 44, 773-780.

Kumar, S., K. M. Pandey and K. K. Sharma (2021). Advances in drag-reduction methods related with boundary layer control – A review. *Materials Today: Proceedings* 45, 6694-6701.

Li, W. (2020). Turbulence statistics of flow over a drag-reducing and a drag-increasing riblet-mounted surface. *Aerospace Science and Technology* 104, 106003.

Li, W. and H. Liu (2019). Two-point statistics of coherent structures in turbulent flow over riblet-

Li, Z., Y. Jin, J. Du, H. Zhang and C. Nie (2021). Physical mechanisms investigation of shark skin-inspired compressor cascade based on

large Eddy simulations. *Journal of Turbomachinery* 143, 061005.

Mele, B. and R. Tognaccini (2018). Slip length–based boundary condition for modeling drag reduction devices. *AIAA Journal* 56, 3478-3490.

Miyazaki, M., Y. Hirai, H. Moriya, M. Shimomura, A. Miyauchi and H. Liu (2018). Biomimetic riblets inspired by shark skin denticles: *Digitizing, modeling, and flow simulation. Journal of Bionic Engineering* 15, 999-1011.

Modesti, D., S. Endrikat, N. Hutchins and D. Chung (2021). Dispersive stresses in turbulent flow over riblets. *Journal of Fluid Mechanics* 917, A55.

Ng, J. H., Jaiman, R. K. and T. T. Lim (2018). On the turbulent flow field over riblets of various groove sizes at low Reynolds number. *arXiv preprint arXiv* 1803, 07283.

Nili-Ahmadabadi, M., O. Nematollahi, K. C. Kim (2019). Effects of coarse riblets on air flow structures over a slender delta wing using particle image velocimetry. *Chinese Journal of Aeronautics* 32, 1367-1379.

Ong, L. and J. M. Wallace (1998). Joint probability density analysis of the structure and dynamics of the vorticity field of a turbulent boundary layer. *Journal of Fluid Mechanics* 367, 291-328.

Perry, A. E. and Hoffmann P. H. (1976) An experimental study of turbulent convective heat transfer from a flat plate. *Journal of Fluid Mechanics* 77, 355-368.

Qiu, H., K. Chauhan and C. Lei (2020). A numerical study of drag reduction performance of simplified shell surface microstructures. *Ocean Engineering* 217, 107916.

Raayai-Ardakani, S. and G. H. McKinley (2019). Geometric optimization of riblet-textured surfaces for drag reduction in laminar boundary layer flows. *Physics of Fluids* 31, 053601.

Rastegari, A. and R. Akhavan (2018) .The common mechanism of turbulent skin-friction drag reduction with superhydrophobic longitudinal microgrooves and riblets. *Journal of Fluid Mechanics* 838, 68-104.

Bhattacharya, S. and A. Ahmed (2020). Effect of aspect ratio on the flow over a wall-mounted hemispherical turret. International *Journal of Heat and Fluid Flow* 84, 108600.

Suzuki, Y. and N. Kasagi (1994). Turbulent drag reduction mechanism above a riblet surface. *AIAA Journal* 32, 1781-1790.

Wallace, J. M. (2016). Quadrant analysis in turbulence Research: History and Evolution. *Annual Review of Fluid Mechanics* 48, 131-58.

Wang, X., Z. Y. Fan, Z. Q. Tang and N. Jiang (2022). Arrayed TRPIV measurement of large-scale coherent motions in turbulent boundary layer. *Acta Aerodynamica Sinica* 40, 49-56.

Wang, X. W., Z. Y. Fan, Z. Q. Tang and N. Jiang (2021). Drag reduction and hairpin packets of the turbulent boundary layer over the superhydrophobic-riblets surface. *Journal of Hydrodynamics* 33, 621-635.

Wu, Z., S. Li, M. Liu, S. Wang, H. Yang and X. Liang (2019). Numerical research on the turbulent drag reduction mechanism of a transverse groove structure on an airfoil blade. *Engineering Applications of Computational Fluid Mechanics* 13, 1024-1035.

Xu, Y., W. Songn and D. Zhao (2018). Efficient optimization of ringlets for drag reduction over the complete mission profile. *AIAA Journal* 56, 1483-1494.

Yan, D., J. Sun, T. Gao, P. Chen, Y. Cheng and W. Chen (2021). Experimental study on the effect of solid particles on ribletplate turbulent boundary layer. Chinese *Journal of Theoretical and Applied Mechanics* 53, 2280-2288.

Yang, S. and N. Jiang (2012). Tomographic TR-PIV measurement of coherent structure spatial topology utilizing an improved quadrant splitting method. *Science China Physics, Mechanics and Astronomy* 55, 1863-1872.

Yang, Y., Y. Liu, R. Liu, C. Shen, P. K. Zhang, R. K. Wei, X. M. Liu and P. W. Xu (2021). Design, validation, and benchmark tests of the aeroacoustic wind tunnel in SUSTech. *Applied Acoustics* 175, 107847.

Yu, C., M. Liu, C. Zhang, H. Yan, M. Zhang, Q. Wu, M. Liu and L. Jiang (2020). Bio-inspired drag reduction: From nature organisms to artificial functional surfaces. *Giant* 2, 100017.

Zhang, M. M., Z. L. Zhang and M. Zhao (2020a). Investigation on the mechanism of drag modification over triangular riblets. *Journal of Applied Fluid Mechanics* 13, 1093-1106.

Zhang, Z., M. Zhang, C. Cai and K. Kang (2020b). A general model for riblets simulation in turbulent flows. *International Journal of Computational Fluid Dynamics* 34, 333-345.